FINAL REPORT
Evaluation of 3D Inverse Code Using Rotor 67 as Test Case

T. Dang
Associate Professor
Department of Mechanical, Aerospace and Manufacturing Engineering
Syracuse University
Syracuse, NY 13244

submitted to

NASA Lewis Research Center
Grant NAG3-1933
Grant Monitor: Dr. D. R. Reddy

2/2/98

Summary

A design modification of Rotor 67 is carried out with a full 3D inverse method. The blade camber surface is modified to produce a prescribed pressure loading distribution, with the blade tangential thickness distribution and the blade stacking line at midchord kept the same as the original Rotor 67 design. Because of the inviscid-flow assumption used in the current version of the method, Rotor 67 geometry is modified for use at a design point different from the original design value. A parametric study with the prescribed pressure loading distribution yields the following results. In the subsonic section, smooth pressure loading shapes generally produce blades with well-behaved blade surface pressure distributions. In the supersonic section, the study shows that the strength and position of the passage shock correlate with the characteristics of the blade pressure loading shape. In general, "smooth" prescribed blade pressure loading distributions generate blade designs with reverse cambers which have the effect of weakening the passage shock.

1. Introduction.

Turbomachine blade design systems usually employ a quasi-3D blade design module to generate the initial blading geometries. This module typically consists of two steps: a flow selection step for each blade row and the blade-geometry definition step. In the first step, a throughflow method with built-in loss correlations is used to select the work or flow-angle distribution (i.e. stagnation enthalpy rise or swirl) for each blade row so as to maximize the efficiency of the multistage machine. This search process is subjected to restrictions placed on the diffusion factor, blade stagger angle, surge margin, and structural integrity. The second step in the quasi-3D blade design module involves the use of families of standard profile shapes with correlated performance or 2D/quasi-3D blade-to-blade design methods (inverse or optimization techniques) to generate the blade geometries.

Following closely the current design practice, we have developed a full 3D inverse method which can readily be integrated into current blade design systems (Dang & Damle, 1996). In this proposed "advanced" design system, we envision that the existing throughflow method would be retained to select the swirl distribution for each blade row. A 3D inverse method is then used to find the blade geometry required to produce the flow conditions selected by the throughflow method.

Inverse methods can be formulated with different choices of prescribed quantities. The two popular choices are (1) the pressure distributions along the blade upper- and lower-surfaces (Demeulenaere & Van den Braembussche, 1996; Giles & Drela, 1987), and (2) the blade pressure loading distribution (i.e. the difference in static pressure between the blade upper- and lower-surfaces), a stacking line (in the 3D case), and the blade thickness distribution (Dang & Damle, 1996; Novak & Haymann-Haber, 1983; Tan et al., 1984). Both approaches have their own advantages and disadvantages. The main issues of concern are the robustness of these formulations in 3D (i.e. existence of solution for arbitrary prescribed quantities), and the compatibility of the method with existing design systems (i.e. relevance between the prescribed flow quantities and the throughflow solutions, and ease of incorporating structural requirements such as minimum blade thickness and stacking location into the inverse method).

The primary prescribed quantities in the 3D inverse method of Dang & Damle (1996) are the blade thickness distribution, the blade pressure loading distribution $\Delta p(r, z)$, and a stacking line. The computed geometrical quantity is the 3D blade camber surface. The design strategy employed in this inverse method is relatively compatible with many blade-generation procedures employed in industry. In many existing design systems, the blade profiles are generated using the following systematic geometrical technique. The blade profile at a given spanwise station is constructed by superimposing a standard profile half-thickness shape (i.e. C4, T4, NACA 0015 base profiles) normal to and on either side of a camber line (usually a circular arc or a parabola). The camber leading- and trailing-edge angles are based on the throughflow solutions, flow-incidence selection, and blade-deviation angle correlations. These 2D blade profiles are then stacked together along a pre-determined stacking line (usually based on structural requirements) to form a 3D blade profile.

Using the 3D inverse method of Dang & Damle (1996), as before, the designer would first select the blade thickness distributions at the computed spanwise stations. Next, instead of generating the 3D blade camber surface using standard camber surface shapes, the camber surface is now computed based on a prescribed blade pressure loading distribution and a specified

stacking line. We note that with this 3D inverse method, flow incidence is indirectly specified through the loading shape (see discussion below), and blade deviation angle is part of the solution.

The shape of the prescribed blade pressure loading Δp (pressure difference between the blade pressure and suction surfaces) is characterized by the following properties (Fig. 1):

- The pressure loading must vanish at the blade leading- and trailing-edges.
- Flow incidence is imposed by forcing a "large" gradient in Δp near the blade leading-edge region. We note that with this 3D inverse method, flow incidence is indirectly specified through the loading shape, and blade deviation angle is part of the solution.

The designer also must specify the magnitude of the prescribed Δp distribution. By considering the θ-momentum equation for a control volume coinciding with a streamtube between the blade leading- and trailing-edges, one can relate Δp to the tangential mass-averaged angular momentum per unit mass $r\bar{V}_\theta$ (Dang, 1995)

$$\int r\Delta p dA_\theta = \dot{m}[(r\bar{V}_\theta)_{TE} - (r\bar{V}_\theta)_{LE}] \tag{1}$$

where $\dot{m}$ is the mass flow rate within the streamtube. Consequently, the area under the $(r\Delta p)$ versus streamwise-distance curve is approximately related to the local overall change in swirl across a blade row. We note that the right-hand-side of Eq. (1) can be approximated using the throughflow solutions by assuming that the "blade" streamlines coincide with the meridional grid lines.

In the inviscid-flow version of the 3D inverse method proposed by Dang & Damle (1996), the unsteady 3D Euler equations are solved using the robust finite-volume time-marching algorithm of Jameson et al. (1981). During this time-marching process, fluid is allowed to cross the blade surfaces, and a pressure-jump condition (i.e. the prescribed blade pressure loading Δp) is imposed across the blade surfaces. The flow-tangency condition along the blade surfaces is then used to calculate the correct blade geometry via an iteration process. The readers are referred to the original papers for the details of the method (Dang, 1995; Dang & Damle, 1996; Dang & Isgro, 1995). The computer code employed in this study, called the INV3D code, can run in both the analysis mode and the inverse mode.

In this report, we use NASA Rotor 67 as a test case to demonstrate this 3D inverse method. We emphasize that the purpose of this study is not to improve the Rotor 67 design, but simply to demonstrate the use of the present 3D inverse method to design a fan rotor. This report is organized as follows. In section 2, we discuss the strategy employed for the redesign of Rotor 67. In section 3, we present the validation work of the INV3D code. In section 4, we summarize the design modification study of Rotor 67 using the INV3D code, including a parametric study with the prescribed loading shape. Finally, concluding remarks are given in section 5.

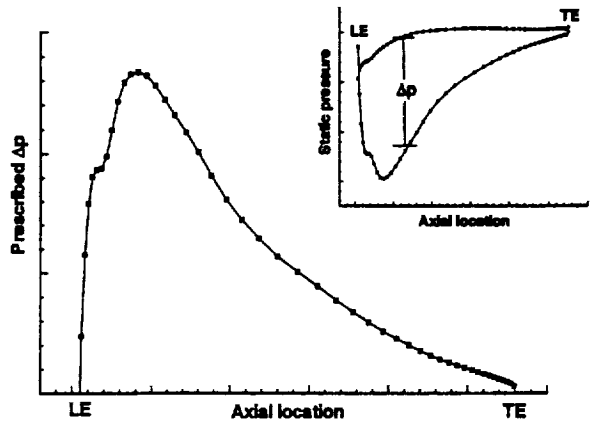

Figure 1: Characteristics of prescribed blade pressure loading Δp.

2. Redesign Strategy for Rotor 67.

In this study, we use the NASA Rotor 67 geometry documented in Strazisar et al. (1989) as the test case for the 3D inverse method. As the present version of the method assumes inviscid flow, the mass flow rate is modified so that the passage shock near the tip region resides in the blade region (Fig. 5). The mass flow rate employed in this study is 35.6 kg/sec (3% higher than the original design value). At this mass flow rate, the total pressure ratio predicted by an inviscid method is 1.81 (10% higher than the original design value). With the blade rotational speed set at 16,000 RPM, the inlet relative Mach number at the rotor tip is 1.45 (5.1% higher than the original design value). The number of blades is kept the same at 22 blades.

At the new operating point, we use the 3D inviscid inverse method to modify the original Rotor 67 design by attempting to (1) minimize adverse pressure gradients on the blade surfaces in the subsonic section of the rotor, and (2) reduce the strength and control the position of the passage shock in the supersonic section of the blade. The design modification is carried out by keeping the blade thickness distribution and the stacking line at midchord the same as the original Rotor 67 design, while the blade pressure loading Δp is modified so as to conserve the area under the $(r\Delta p)$ versus axial-distance curves at all spanwise locations. This constraint will ensure that the modified rotor has roughly the same work distribution as the original Rotor 67 design.

3. Consistency Check of INV3D Code

We first present the validation study of the INV3D code running in the analysis mode against Adamczyk et al. (1989) analysis code (Euler option). Both codes are used to analyze the flow through the original Rotor 67 geometry at the new operating point with a mesh size of 120 cells in the axial directions, 32 cells in the spanwise direction, and 24 cells in the pitchwise direction. Figure 2 shows the comparison of the static pressure distributions along the blade surface at the 25% and 75% spanwise locations at the design mass flow rate. This figure shows very good agreement between the two codes running in the analysis mode.

Next, we present the validation study of the INV3D code running in the inverse mode. In this investigation, we attempt to reproduce the original Rotor 67 geometry using the blade pressure loading Δp computed by the analysis mode of the INV3D code. Figure 3 shows the comparison of the axial distributions of the blade wrap angle (tangential coordinate of the blade camber surface) and the blade angle at three spanwise locations between the original Rotor 67 geometry and the blade geometry computed by the INV3D code running in the inverse mode. This figure shows that the inverse method successfully reproduces the Rotor 67 geometry. Small discrepancies in the blade angle are found near the blade leading- and trailing-edges, which are primarily due to the small oscillations in both the input blade pressure loading (calculated using the analysis mode of the INV3D code) and the flow solutions occurring at these locations. In particular, as the blade surface velocities are used to trace out the camber surface (Dang & Damle, 1996), dispersion errors in the flow solution will result in oscillations in the blade angle.

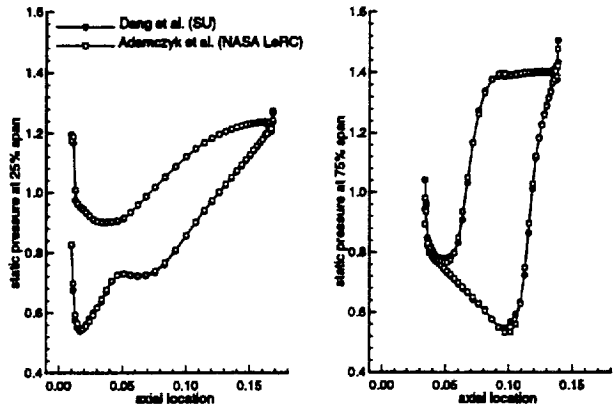

Figure 2: Validation of INV3D code running in analysis mode.

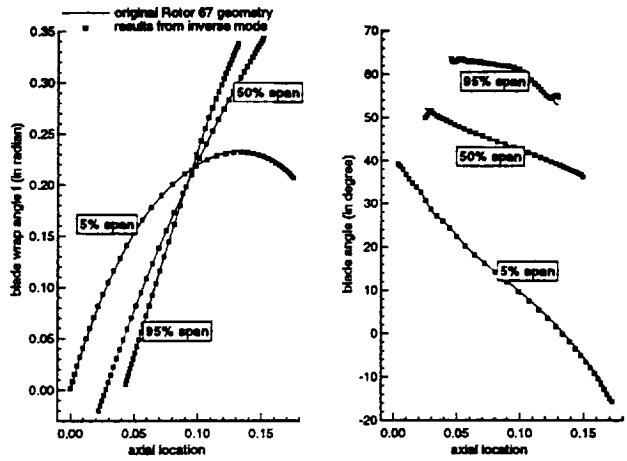

Figure 3: Validation of INV3D code running in inverse mode.

4. Redesign of Rotor 67

In this section, we present several modifications of Rotor 67 using the 3D inverse method. Figure 4 (Rotor 67) shows the blade pressure loading contour computed by the INV3D code (analysis mode) for the original Rotor 67 geometry at the new operating point. The figure shows two strong discontinuities in the tip region. Examinations of the static pressure contours on the blade pressure and suction surfaces clearly show that the two discontinuities correspond to the passage shock (Fig. 5 - Rotor 67). The first discontinuity corresponds to the passage shock impinging on the blade pressure surface, while the second discontinuity corresponds to the passage shock impinging on the blade suction surface. This can be seen clearly from the static-pressure contour plot at the 85% span location shown in Fig. 6. In terms of the quality of this blade design, Figs. 5 and 6 indicate that the axial position of the passage shock is farther downstream than desired (a consequence of the inviscid-flow assumption).

The x-y plots shown in Fig. 6 (static pressure and pressure loading Δp) indicate that at the new operating point, Rotor 67 is front-loaded near the hub with large flow incidence, while the blade is rear-loaded near the tip with nearly zero incidence. At the 15% span location where the inflow Mach number is 0.8, the "wavyness" in the loading shape near the leadinge-edge region correlates with the undesirable static-pressure behavior along the blade suction surface. At the 85% span location where the inflow Mach number is 1.32, the locations of the two discontinuities in the loading shape at the 40% and 95% chord locations coincide exactly with the two discontinuities in the blade-surface static pressure distributions. They also coincide with the location of the passage shock shown in the static pressure contour plot in the blade-to-blade plane.

The observations outlined above suggest that a "smooth" blade pressure loading distribution may correspond to better static pressure distributions on the individual blade surfaces than a "wavy" one or one with discontinuities. Another concern is the position of the passage shock. At the design operating point, the desired axial position of the passage shock is inside the blade row. Figures 5 and 6 indicate that any attempt to improve Rotor 67 for the new operating flow regime should move the passage shock further upstream. In an attempt to quantify the relationship between the blade loading shape and the position/strength of the passage shock in the supersonic section of the blade, we examine four families of loading shapes. We summarize this parametric study with the following four specific examples. We note that the following inverse calculations are carried out at approximately the same mass flow rate and overall change in stagnation enthalpy.

Consider the Type D loading shape. The shape is characterized by the presence of two discontinuities, similar to a "square wave" shape. Figure 7 shows an example of the Type D loading where the two discontinuities are located at the 20% and 80% chord locations. We note that the original Rotor 67 geometry is a Type D design in the tip region (for example, at the 85% span location, the two discontinuities are located at the 40% and 95% chord locations). As expected, the inverse calculation yields a new blade profile which places the passage shock inside the blade row at roughly the 20% and 80% chord locations! The blade-surface static pressure contour plots (Fig. 5) clearly show that the passage shock impinges on the blade pressure and suction surfaces at approximately the 20% and 80% chord locations, respectively. We also observe that this type of loading is unsuitable in the subsonic section of the blade.

Consider the Type $\dot{S}$ loading shape. The shape is characterized by a "smooth" curve where steep gradient is absent. This type of loading is nearly symmetrical about the midchord location. Shown in Fig. 8 is an example of such loading shape. It is basically the Type D loading shape

shown in Fig. 7, but with the two discontinuities smoothed out. With a Type S loading shape, we expect that the passage shock present in the previous Type D design will be smeared out and becomes a "near isentropic" compression-wave system. This is clearly shown in the static pressure contour plot at the 85% span location (Fig. 8). We note that the compression near the leading-edge region along the blade pressure surface corresponds to the gradient in the loading shape between the leading edge and the 20% chord location, while the compression occuring near the trailing edge along the blade suction surface corresponds to the gradient in the loading shape between the 80% chord location and the trailing edge. Figure 5 shows that the passage shock has almost disappeared on both the blade suction and pressure surfaces, except for a very small region near the tip.

Consider the Type F loading shape. The shape is characterized by a steep gradient near the blade leading edge and corresponds to a front-loaded design. Figure 9 is an example of the Type F loading which corresponds to a finite-incidence blade design used in many preliminary design calculations ($\Delta p \sim cos[\pi X/2]$ where $X \equiv [z - z_{LE}]/[z_{TE} - z_{LE}]$). Relative to the Type D design, the discontinuity in the front portion of the Type D loading shape is retained, while the discontinuity in the rear portion has been smoothed out. Consequently, since the first discontinuity corresponds to the passage shock meeting the blade pressure surface and the second discontinuity corresponds to the pasage shock meeting the blade suction surface, we expect that the passage shock remains strong near the blade pressure surface, while it weakens as it impinges on the blade suction surface. This exact flow pattern occurs when an inverse calculation is performed with a Type F loading, as can be seen from the static-pressure contour plot at the 85% span location shown in Fig. 9 and on the blade surfaces shown in Fig. 5. We note that the large discontinuity in the loading shape at the blade leading edge (i.e. finite incidence design) has pushed the passage shock forward of the blade, as can be seen by the absence of the shock wave on the blade pressure surface shown in Fig. 5. We also note that the Type F loading yields well-behaved static pressure distributions along the blade surfaces in the subsonic section of the blade (Fig. 9).

Consider the Type R loading shape. The shape is characterized by a steep gradient near the blade trailing edge and corresponds to a rear-loaded design. Figure 10 is an example of the Type R loading. Relative to the Type D design, the discontinuity in the front portion of the Type D loading shape is smoothed out, while the discontinuity in the rear portion is retained. Consequently, we expect that the passage shock weakens as it impinges on the blade pressure surface, while it remains strong near the blade suction surface. This exact flow pattern occurs when an inverse calculation is carried out with a Type R loading, as can be seen from the static-pressure contour plot at the 85% span location shown in Fig. 10 and on the blade surfaces shown in Fig. 5. A near isentropic compression is observed along the blade pressure surface, while a shock wave occurs near the trailing edge along the blade suction surface.

Figure 11 shows a comparison of the blade angle distributions, including x-y plots at the 15%, 50%, and 85% span locations. The original Rotor 67 blade geometry is smooth, with the blade angle decreasing monotonically from the leading- to the trailing-edge values. On the other hand, the blade geometries generated by the 3D inverse method all have "wavy" distributions. The most interesting feature is the reverse camber (or negative camber) effect in the supersonic section of the blades (Prince, 1980; Dang, 1995). We note that the region of reverse camber coincides with the axial location where the passage shock weakens as it impinges on the blade suction surface (Type S and Type F loading shapes) or the blade pressure surface (Type R loading shape). In the Type D case, the discontinuities in the loading shape produce two kinks in the

blade geometry. Finally, we note again the presence of oscillations in the blade angle distributions near the leading- and trailing-edge regions due to the presence of oscillations in the flow solutions. We also note the rather large differences in the blade angle at the leading- and trailing-edges. This is due to the fact that these blades are designed with different flow incidence, and the deviation angle at the blade trailing edge can be different between these designs because of the various choices of blade loading shapes and the slight difference in radial work distribution.

Based on this parametric study, we present a final blade design which employs different loading shapes along the blade span. At the hub location, a front-loaded design with finite incidence is used (Type F loading shown in Fig. 9). This type of loading was shown to yield well-behaved static pressure distributions along the blade surfaces in the subsonic section of the blade. At the midspan station, a smooth (Type S) loading shape is used, with allowance for a small flow incidence. This will ensure that the passage shock in this low supersonic-flow section of the blade is not detached from the blade leading edge. At the tip location, the same Type S loading shape with zero incidence shown in Fig. 8 is employed to ensure that the passage shock is weak and resides inside the blade row. The contour plot of the prescribed blade loading for the modified design is shown in Fig. 4. The back pressure was adjusted so that the design mass flow rate is met. By matching the area under the $(r\Delta p)$ versus streamwise-distance curve at all spanwise locations, the modified design has 1.5% higher change in $r\bar{V}_\theta$, and the stagnation pressure ratio is 2.0% higher than the original Rotor 67 design.

Figure 12 gives a comparison of the 3D blade geometries. This figure indicates that the original Rotor 67 blade and the modified blade are very similar, with the latter appearing to have more turning in the hub region. In actuality, the original Rotor 67 design is rear-loaded while the modified design is front-loaded, and this difference results in higher variation in the blade wrap angle for the modified design than the original design.

Examinations of the 3D solutions show that the flow feature in the subsonic section of the modified blade is very similar to the Type F results shown in Fig. 9. One interesting new flow feature is the effect of small flow-incidence imposed in the low supersonic-flow section of the blade. Figure 13 illustrates a comparison of the flow solutions between Rotor 67 and the modified design at the 60% span location where the inflow Mach number is 1.13. The figure clearly shows the small incidence imposed at the blade leading edge, which results in the placement of a weak shock near the blade leading edge along the blade pressure surface. Figure 14 illustrates a similar comparison of the flow solutions at the 90% span location where the inflow Mach number is 1.35. At this span location, the use of the Type S (smooth) loading shape and zero incidence design condition has weakened the passage shock considerably (as confirmed by inspection of the entropy plot). On the other hand, the original Rotor 67 blade, which corresponds to the Type D design in the supersonic section, has a strong passage shock located near the trailing edge.

Finally, we present a consistency check for one of the modified blades. Here, we calculate the flowfield through the modified blade using the analysis mode of the INV3D code and compare the solution against that given by the inverse mode. As the modified design is close to the shock-free condition, the solution is sensitive to small changes in flow conditions. Figure 15 shows the comparisons of the pressure distributions along the blade surfaces and the axial distribution of $r\bar{V}_\theta$ at the 25% and 75% span locations for the Type F design shown in Fig. 9. These figures confirm the flow characteristics of the modified blade design presented earlier. We note that in order to match the solutions given by the inverse and analysis modes, the back pressure had to

be slightly adjusted. The two solutions are matched when p_{back}/P_{01} at the hub is set to 1.080 in the inverse mode and 1.083 in the analysis mode (0.28% error). The calculated mass flow rate is 35.87 kg/sec for the inverse mode and 36.03 kg/sec for the analysis mode (0.46% error), while the mass-averaged stagnation pressure ratio is 1.804 for the inverse mode and 1.809 for the analysis mode (0.28% error).

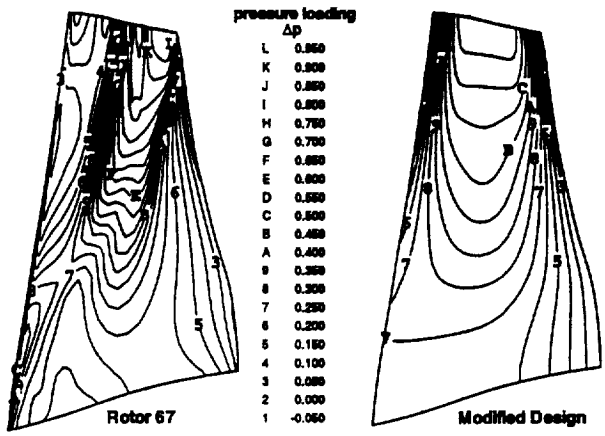

Figure 4: Comparison of blade pressure loading Δp.

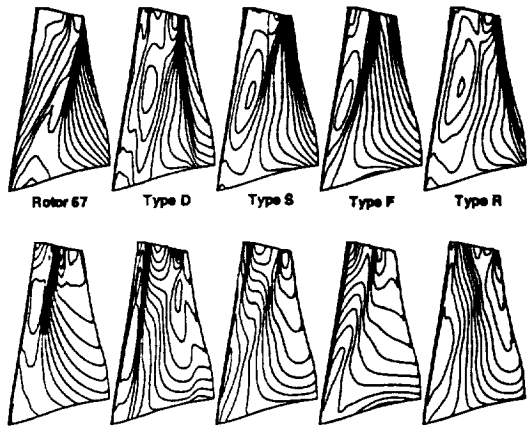

Figure 5: Comparison of static pressure contour on suction (top) and pressure (bottom) surfaces.

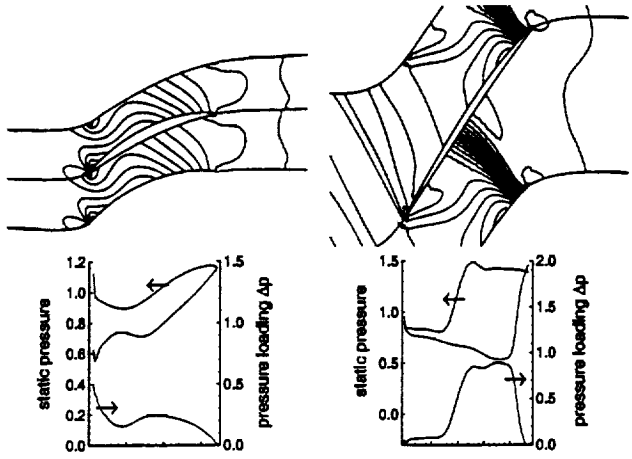

Figure 6: Rotor 67 - flow solutions at 15% and 85% span locations.

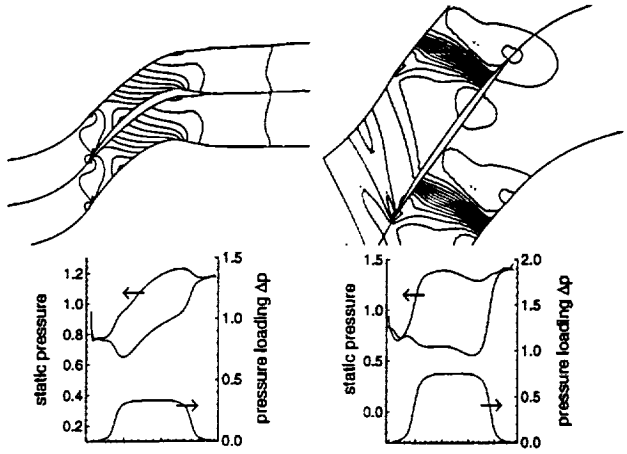

Figure 7: Type D loading - flow solutions at 15% and 85% span locations.

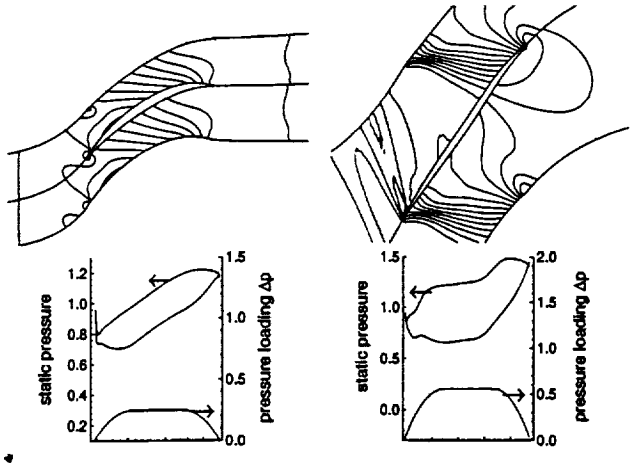

Figure 8: Type S loading - flow solutions at 15% and 85% span locations.

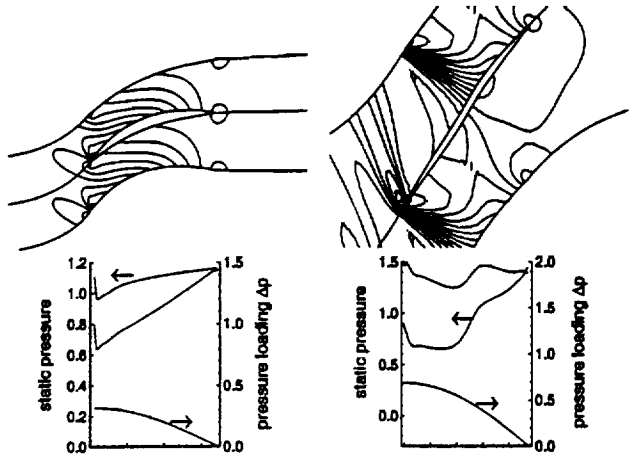

Figure 9: Type F loading - flow solutions at 15% and 85% span locations.

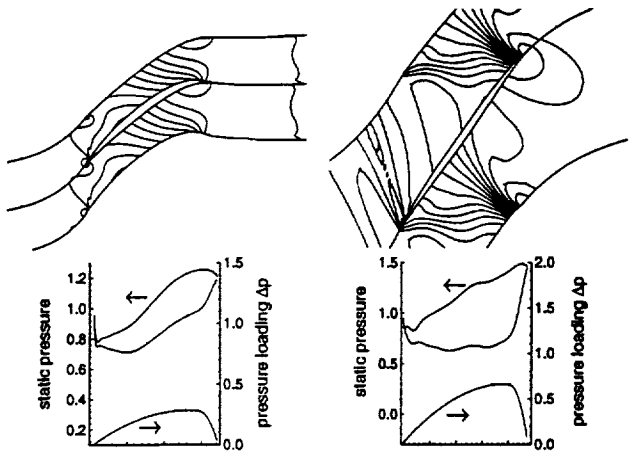

Figure 10: Type R loading - flow solutions at 15% and 85% span locations.

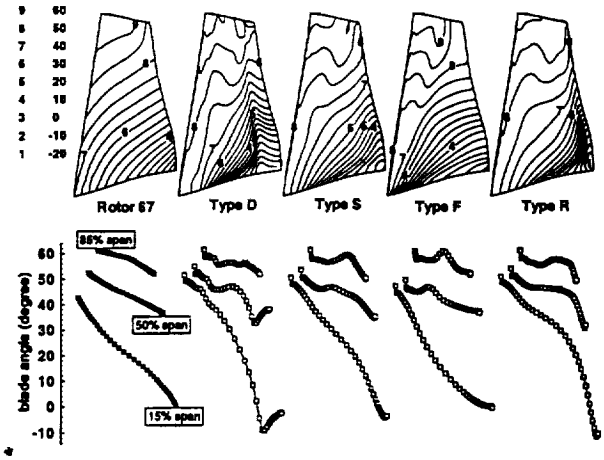

Figure 11: Comparison of blade angle distributions.

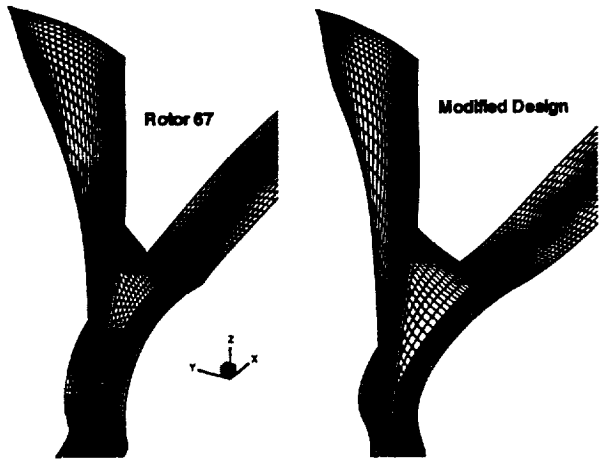

Figure 12: Comparison of 3D blade geometry.

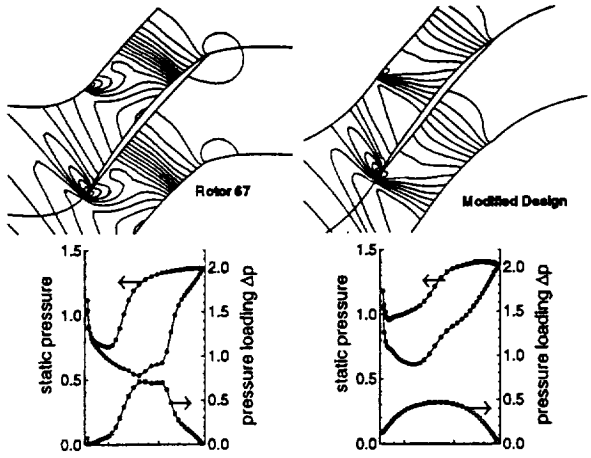

Figure 13: Flowfield comparison at 60% span location.

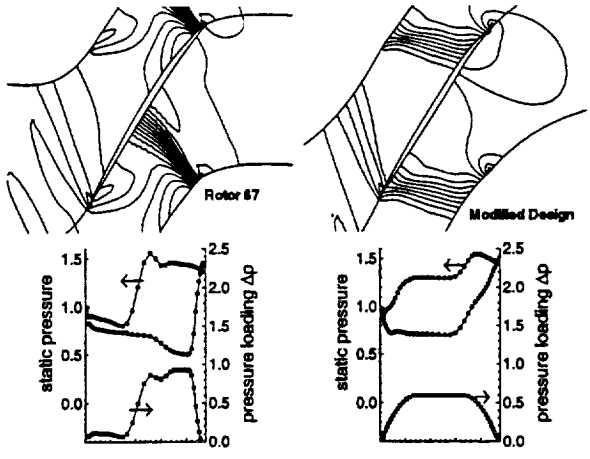

Figure 14: Flowfield comparison at 90% span location.

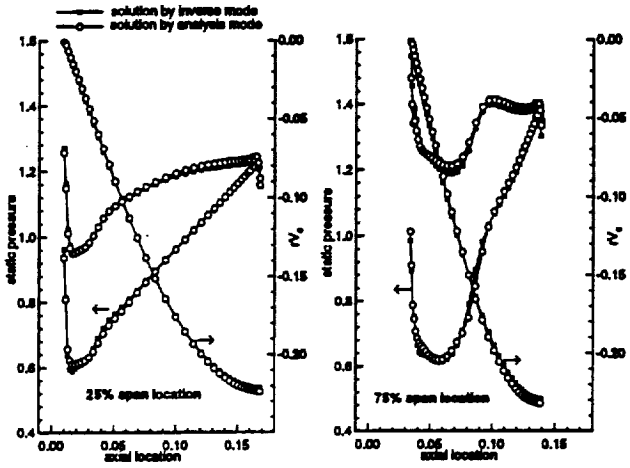

Figure 15: Comparison of static pressure and swirl at 25% and 75% span locations.

5. Conclusion

A 3D inviscid inverse method is used to redesign NASA Rotor 67 for a frictionless-flow environment. The redesign is carried out by modifying the prescribed pressure loading shape such that the radial work distribution and the overall change in $r\bar{V}_\theta$ across the rotor is preserved. In this study, we elect to keep the blade thickness distribution and the blade stacking at the midchord location the same as the original Rotor 67 design.

Based on a parametric study carried out with four distinct families of loading shapes, the following conclusions can be made. In the subsonic section of the blade, the Type F (front-loaded) or Type S (smooth and nearly symmetrical) loading shape should be employed, depending on the requirement of flow incidence at the design point. In the supersonic section of the blade, the position of the passage shock correlates with the blade loading shape. In general, a shock wave will appear at the location where the gradient in the loading shape curve is "steep." For example, a "square wave" (Type D) loading shape will result in a strong passage shock, and the location of the passage shock coincides with the the two discontinuities in the square wave. On the other hand, front-loaded (Type F) and rear-loaded (Type R) blade designs place one end of the passage shock near the blade leading- and trailing-edges, respectively, while the other end weakens significantly as it impinges on the neighboring blade. The weakening of the passage shock is achieved through reverse cambering. When incidence is imposed, the discontinuity in the loading shape at the blade leading edge pushes the passage shock upstream of the blade passage.

Because of the inviscid-flow assumption employed in this study, this work is regarded as a stepping-stone towards a practical design method, and no attempt was made at evaluating the goodness of the modified blades at the off-design conditions. We plan to carry out a similar redesign study of Rotor 67 at the actual operating point (including an off-design evaluation study) when the viscous version of the inverse method is available.

References

Adamczyk, J.J., Celestina, M.L., Beach, T.A. and Barnett, M., 1989, "Simulation of 3D Viscous Flow Within a Multistage Turbine," *ASME Journal of Turbomachinery*, vol. 112, pp. 370-376.

Dang, T.Q., 1995, "Inverse Method for Turbomachine Blades Using Shock-Capturing Techniques," AIAA Paper 95-2465.

Dang, T. and Isgro, V., 1995, "Euler-Based Inverse Method for Turbomachinery Blades - Part 1: Two-Dimensional Cascades," *AIAA Journal*, vol. 115, no. 12, pp. 2309-2315.

Dang, T. and Damle, S., 1996, "Euler-Based Inverse Method for Turbomachinery Blades - Part 2: Three Dimensions," submitted to *AIAA Journal*.

Demeulenaere, A. and Van den Braembussche, R., 1996, "Three-Dimensional Inverse Method for Turbomachinery Blading Design," ASME Paper 96-GT-39.

Giles, M. and Drela, M., 1987, "Two-Dimensional Aerodynamic Design Method," *AIAA Journal*, vol. 25, pp. 1199-1205.

Jameson, A., Schmidt, W. and Turkel, E., 1981, "Numerical Solutions of the Euler Equations by Finite Volume Methods Using Runge-Kutta Time Stepping Schemes," AIAA Paper 81-1259.

Novak, R.A. and Haymann-Haber, 1983, "A Mixed-Flow Cascade Passage Design Procedure Based on a Power Series Expansion," *Journal of Engineering for Power*, vol. 105, pp. 231-242.

Prince, D.C., 1980, "Three-Dimensional Shock Structures for Transonic/Supersonic Compressor Rotors," *AIAA Journal of Aircraft*, vol. 17, pp. 28-37.

Strazisar, A., Wood, J., Hathaway, M. and Suder, K., 1989, "Laser Anemometer Measurements in a Transonic Axial-Flow Fan Rotor," NASA Technical Paper 2879, Nov. 1989.

Tan, C.S., Hawthorne, W.R., McCune, J.E., Wang, C., 1984, "Theory of Blade Design for Large Deflections: Part 2 - Annular Cascades," *ASME Journal of Engineering for Gas Turbine and Power*, vol. 106, pp. 354-365.